

# Nonlinear Dynamics, Avalanches and Noise For Driven Wigner Crystals

C. Reichhardt and C. J. O. Reichhardt  
*Theoretical Division and Center for Nonlinear Studies,  
Los Alamos National Laboratory,  
Los Alamos, New Mexico 87545, USA*

(Dated: August 8, 2022)

We consider the driven dynamics of Wigner crystals interacting with random disorder. Using numerical simulations, we find a rich variety of transport phenomena as a function of charge density, drive, and pinning strength. For weak pinning, the system forms a defect free crystal that depins elastically. When the pinning is stronger, a pinned glass phase appears that depins into a filamentary flow state, transitions at higher drives into a disordered flow phase, and finally forms a moving smectic. Within the filamentary flow phase, the conduction curves can show switching dynamics as well as negative differential conductivity in which switching events cause some flow channels to be blocked. The velocity noise in the filamentary flow regime exhibits narrow band characteristics due to the one-dimensional nature of the motion, while the moving smectic has narrow band velocity noise with a washboard frequency. In the disordered flow state, the noise power reaches a peak value and the noise has a  $1/f$  character. Our transport results are consistent with recent experimental transport studies in systems where Wigner crystal states are believed to be occurring. Below the conduction threshold, we find that avalanches with a power law size distribution appear when there are sudden local rearrangements of charges from one pinned configuration to another.

## I. INTRODUCTION

There is a broad class of particle like systems that exhibit transitions from pinned to sliding states as function of driving when the particles are coupled to a random substrate<sup>1</sup>. Some examples include depinning of vortices in type-II superconductors<sup>1,2</sup>, colloidal particles driven over rough landscapes<sup>3,4</sup>, frictional systems<sup>5</sup>, magnetic skyrmions<sup>6,7</sup>, and active matter<sup>8,9</sup>. In these systems, there is a critical threshold force that must be applied in order for the particles to remain in continuous motion. If the quenched disorder is weak, the depinning transition can be elastic, with all of the particles maintaining the same neighbors. In contrast, for strong quenched disorder, the depinning becomes plastic and the system breaks up or phase separates into moving and pinned regions<sup>1</sup>. Even when the quenched disorder is very strong, at higher drives it is possible for a dynamic reordering transition to occur into a moving anisotropic crystal<sup>1,10</sup> or moving smectic state<sup>10-12</sup>. The shape of the velocity-force curves near depinning varies depending on whether the depinning is elastic or plastic or if thermal creep comes into play<sup>1</sup>. In some cases, the depinning curves are smooth and have the form  $V \propto (F_D - F_c)^{\beta}$ <sup>1,13,14</sup>, where  $V$  is the velocity,  $F_D$  is the driving force, and  $F_c$  is the depinning threshold. In a two-dimensional (2D) system, the elastic depinning exponent  $\beta = 2/3$ , while for plastic depinning,  $1.25 < \beta < 2.0$ . At higher drives, one or more peaks can appear in the  $d\langle V \rangle/dF_D$  curves, serving as signatures of different dynamical transitions.

In the plastic flow regime, an open question is whether there can be different types of coexisting flow states, such as plastic flow that is fluctuating or plastic flow that forms specific stable structures. If so, this would imply that additional transitions are possible between different

types of plastic flow. For example, one form of plastic flow could be dominated by a finite number of filamentary flow channels. If the filamentary structures change, the velocity-force curves would not be smooth but would show switching behavior with a series of jumps corresponding to the drives at which different channels of motion open for flow<sup>1,15,16</sup>. Switching effects and negative differential conductivity occur in systems such as sliding charge density waves<sup>17</sup>, superconducting vortices in mesoscopic channels<sup>16,18</sup> or near the peak effect<sup>19</sup>, and electron liquid crystals<sup>20,21</sup>; however, it is not well understood how these effects are connected to plastic flow, which often produces nonlinear but smooth velocity-force curves.

Depinning and different sliding phases can also be explored by measuring noise fluctuations, which can show distinctive features such as broad band noise in strongly plastic regimes<sup>1,12,22</sup> or narrow band noise<sup>1,12,23-25</sup> when the system forms a moving crystal. Other studies have shown that transitions from ordered to disordered states are associated with a shift from narrow to broad band noise signatures<sup>20,26-28</sup>.

Another example of systems that can exhibit a variety of threshold and switching behaviors is Wigner crystals<sup>29-42</sup> and electron liquid crystals<sup>20,21,28,43-49</sup>. Wigner crystals can arise in a number of 2D systems, and the appearance of a threshold for conduction has been interpreted as the depinning of Wigner crystals. More recently, a study of the sliding of Wigner crystals or electron solids for varied carrier concentrations in Ref.<sup>37</sup> showed that the depinning threshold decreases with increasing carrier density, and that there can be a two step depinning process followed by a cusp above which the current increases linearly with increasing drive. In this same work, there was a peak in the noise power near

depinning as well as  $1/f$  noise characteristics.

Evidence for Wigner crystal formation has been found with numerous resonance experiments<sup>50–54</sup>, magnetoresistance measurements<sup>55–58</sup>, and commensurability oscillations for composite fermions encircling charges in a Wigner crystal<sup>59</sup>. Several experiments have shown finite depinning thresholds accompanied by negative differential resistance in which the conduction drops with increasing drive<sup>60,61</sup>. There has also been work on 2D metal-insulator transitions suggesting that the system could be forming a Wigner crystal<sup>62–64</sup> or a mixed Wigner crystal and fluid state<sup>65,66</sup>, and the noise behavior is consistent with what is seen for models of transitions from Wigner crystals to Wigner glasses in the presence of quenched disorder<sup>67</sup>.

More recently, evidence for Wigner crystals has been found in monolayer semiconductors and dichalcogenide monolayers<sup>68</sup>, moiré heterostructures<sup>69</sup>, and oxides<sup>70</sup>, while evidence for bilayer Wigner crystals appears in dichalcogenide heterostructures<sup>71</sup>. There have also been several predictions for Wigner crystal formation in the insulating states of moiré systems<sup>70,72</sup>. New methods have recently been developed for creating high quality 2D electron systems that should allow for easier access to Wigner crystal states<sup>73</sup>. A major question is what is the role of quenched disorder in Wigner crystal phases and dynamics, and how it can be determined if a system is in a Wigner crystal, Wigner glass, or fluid state<sup>74</sup>.

Given the recent evidence for Wigner crystal formation and the ubiquity of disorder in most of these systems, it is interesting to study in detail the different possible threshold behaviors and charge flow patterns for a Wigner crystal coupled to disorder to see if there are distinct phases, or whether effects such as switching, negative differential conductivity, and transitions among narrow band and broad band noise characteristics can occur.

Here we examine the driven dynamics of a Wigner crystal interacting with random quenched disorder using molecular dynamics simulations. Previous work employing this approach focused on the depinning threshold and how it changes as a transition occurs from an ordered crystal to a defected solid as a function of increasing quenched disorder strength<sup>34,75</sup>. Other work focused on the dynamic ordering transition from a plastically flowing crystal into a dynamically ordered moving crystal or smectic state for increasing drive<sup>35</sup>, similar to the dynamic ordering found in driven superconducting vortex lattices<sup>10–12</sup>. In additional studies, the change in the noise fluctuations across a pinned Wigner glass to fluid state transition was examined<sup>67</sup>. More recently, molecular dynamics simulations were used to explore the impact of the magnetic field on the sliding dynamics of Wigner crystals, and it was shown that the system has a velocity-dependent Hall angle due to a side jump effect of the charges moving over the pinning sites<sup>76</sup>, similar to the velocity-dependent Hall angle observed in magnetic skyrmion systems with pinning<sup>6,7,77</sup>.

In this work we focus on the Wigner crystal dynam-

ics for both elastic and plastic depinning. When the quenched disorder is strong, a disordered state appears that can depin into a filamentary flow phase where the motion occurs in quasi-one-dimensional (q1D) rivers or channels. The opening of these channels leads to jumps in the conduction, and in some cases, the motion decreases with increasing drive due to the closing of a flow channel, leading to negative differential conductivity. We find that the conduction threshold decreases with increasing carrier density as a result of the appearance of interstitially pinned charges that are immobilized only by the repulsion from other charges and not directly by a pinning site. This occurs once the charge density is high enough that the strongest pinning sites are fully occupied by charges. When a sudden drive is applied in the filamentary flow regime, a strongly fluctuating transient state can appear before the system settles into well defined flowing filaments with a low frequency narrow band noise signal. At higher drives, the filamentary flow is replaced by a strongly fluctuating state in which the noise has a low frequency  $1/f^\alpha$  character with an exponent  $\alpha = 0.7$  that is close to the value found in recent experiments<sup>37</sup>. At higher frequencies, the noise signature has a  $1/f^2$  form. The overall noise power at a specific frequency shows a strong peak just above the conduction threshold, similar to what is observed in recent experiments<sup>37</sup>. For even higher drives, the noise power is reduced and narrow band noise appears when the system enters a moving smectic or moving crystal state. In the strong pinning regime there can be a three step depinning process in which filamentary flow is followed by a nonlinear regime and then by a cusp above which the velocity increases linearly with drive, similar to transport curves obtained in recent experiments<sup>37</sup>.

In the pinned state, as the drive is increased below the threshold for plastic flow, there can be sudden bursts of motion or avalanches in the form of q1D flowing channels of different lengths. The sizes  $s$  of these avalanches are power law distributed according to  $P(s) \propto s^{-1.7}$ . In the elastic pinning regime, the system forms a crystal and depins without the generation of topological defects, and there is no switching behavior or filamentary flow. In the plastic depinning regime, the Wigner crystal exhibits a narrow band noise signal just above the depinning threshold.

## II. SIMULATION AND SYSTEM

We consider a 2D system of size  $L \times L$  with periodic boundary conditions in the  $x$  and  $y$  directions containing  $N$  classical electrons or charges that couple to quenched disorder. The charge density is  $n = N/L^2$  and we set  $L = 36$ . After obtaining an initial configuration via simulated annealing, we increase the driving force from zero in small increments applied over fixed windows of time in order to observe any transient motion that occurs. The first drive that is strong enough to produce continuous motion is

defined to be the conduction threshold.

The equation of motion for charge  $i$  in the Wigner crystal is

$$\alpha_d \mathbf{v}_i = \sum_{j \neq i}^N \nabla U(r_{ij}) + \mathbf{F}_p + \mathbf{F}_D, \quad (1)$$

where  $\alpha_d$  is the damping constant. The charge-charge interaction potential  $U = e^2/r_{ij}$ , where  $r_{ij} = |\mathbf{r}_i - \mathbf{r}_j|$  is the distance between electrons located at  $\mathbf{r}_i$  and  $\mathbf{r}_j$ , and  $e$  is the electronic charge. The pinning force  $\mathbf{F}_p$  is modeled as arising from  $N_p$  short range parabolic traps of finite radius  $r_p$  that exert a maximum confining force of  $F_p$  on a charge, while the driving force  $\mathbf{F}_D = F_D \hat{\mathbf{x}}$  models an externally applied electric field. The pinning density  $n_p = N_p/L^2$  is fixed to  $n_p = 0.25$ . We define the filling fraction  $F = N/N_p$  to be the ratio of the number of charges to the number of pinning sites. Since the charge-charge interactions are long range, we employ a Lekner summation technique for computational efficiency as used in previous studies of particles with Coulomb interactions<sup>35,67,76</sup>. We also note that if the charges are in a magnetic field, their motion is subjected to a Hall angle produced by the Magnus force  $e\mathbf{B} \times \mathbf{v}_i$ . In general, this term is small, and in previous work it was shown that the effect of the Magnus force is particularly weak near the conduction threshold<sup>76</sup>. Since we focus specifically on the conduction threshold in this work, we neglect the Magnus force.

We consider a range of pinning forces, charge densities, and drive values, and employ two types of driving protocols. In the first, the drive is continuously increased by small increments to mimic an experimental velocity-force curve in which a current is swept from zero up to a final value. In the second, we apply a constant drive and hold the drive fixed for an extended period of time. The latter approach allows us to obtain long time series for examining conduction noise. For the continuous sweep protocol, we increase the external drive in increments of  $\Delta F_D = 0.0001$  and wait 18400 simulation time steps before applying the next increase. At each drive increment we measure the average velocity per charge in the driving direction,  $\langle V_x \rangle = N^{-1} \sum_i^N \mathbf{v}_i \cdot \hat{\mathbf{x}}$ . We also calculate the average perpendicular velocity,  $\langle V_y \rangle = N^{-1} \sum_i^N \mathbf{v}_i \cdot \hat{\mathbf{y}}$ , as well as the standard deviations of the velocities for both directions,  $\delta V_x = \sqrt{[\sum_i^N (\mathbf{v}_i \cdot \hat{\mathbf{x}})^2 - \langle V_x \rangle^2]/N}$  and  $\delta V_y = \sqrt{[\sum_i^N (\mathbf{v}_i \cdot \hat{\mathbf{y}})^2 - \langle V_y \rangle^2]/N}$ . In certain regimes, we increase the waiting time in order to obtain smoother curves for calculating  $d\langle V_x \rangle/dF_D$ . This increase also allows us to clearly delineate bursts or avalanches of motion.

### III. SWITCHING AND CONDUCTION

In Fig. 1(a) we plot the velocity  $\langle V_x \rangle$  versus the driving force  $F_D$  for a system with a pinning strength of  $F_p = 0.5$

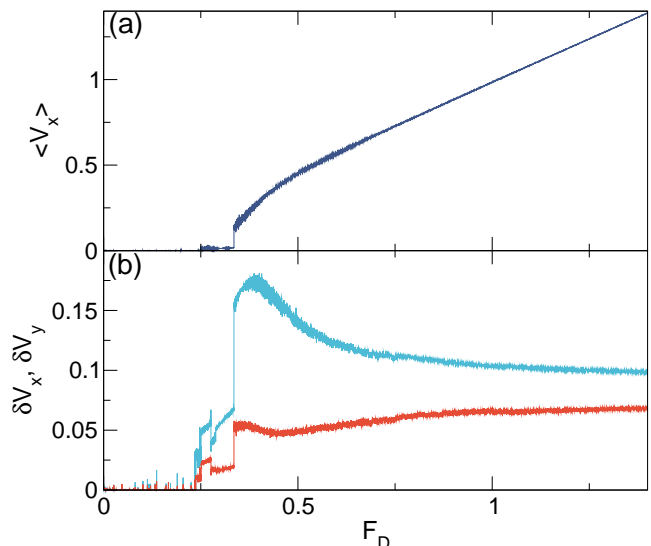


FIG. 1: (a) The velocity  $\langle V_x \rangle$  in the driving direction vs the driving force  $F_D$  for a system with a filling factor of  $F = 0.4$  and a pinning force of  $F_p = 0.5$ . The onset of conduction occurs near  $F_D = 0.35$ . (b) The corresponding standard deviations of the velocity parallel,  $\delta V_x$  (blue), and perpendicular,  $\delta V_y$  (red), to the driving direction vs  $F_D$  for the same system, showing a pinned regime and a filamentary flow regime for drives below the jump into the disordered flow regime.

and a filling fraction of  $F = 0.4$  under a continuously increasing drive. A clear conduction threshold appears near  $F_D = 0.34$ . In Fig. 1(b) we plot the corresponding standard deviations of the velocities parallel,  $\delta V_x$ , and perpendicular,  $\delta V_y$ , to the drive versus  $F_D$ . These curves show more clearly that below the conduction threshold, for  $0.24 < F_D < 0.34$ , there are a series of jumps in the velocity fluctuations in both the  $x$  and  $y$  directions, while at  $F_D = 0.34$  there is a large peak in  $\delta V_x$  at the transition to the plastic or continuously fluctuating disordered flow phase. In general,  $\delta V_y < \delta V_x$ . For  $F_D > 0.65$ , there is an ordering into a moving smectic phase. The onset of this transition extends down to  $F_D > 0.4$ , where  $\delta V_x$  begins to drop as the flow gradually becomes less disordered and the smectic state emerges.

In Fig. 2(a,b) we show a closeup of  $\langle V_x \rangle$ ,  $\delta V_x$ , and  $\delta V_y$  versus  $F_D$  for the system from Fig. 1. There is a pinned regime for  $F_D < 0.24$  in which  $\langle V_x \rangle = 0$ , followed by what we call the filamentary flow phase for  $0.24 < F_D < 0.34$ . We note that even within the pinned phase, there are still a number of isolated jumps in all three quantities that correspond to avalanches involving the correlated motion of multiple charges when the drive is increased. At  $F_D = 0.25$ , there is a large jump in  $\langle V_x \rangle$  followed by a region in which  $\langle V_x \rangle$  increases linearly with increasing  $F_D$ . This is followed by a jump down in  $\langle V_x \rangle$  and then by a smaller and a larger jump up. Counterparts to these jumps also appear in  $\delta V_x$  and  $\delta V_y$ . The upward jumps are associated with switching events in which well defined channels of motion appear, while downward jumps occur

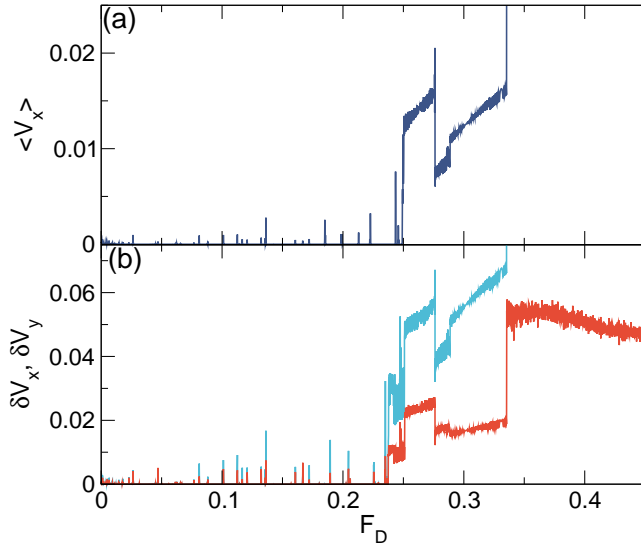


FIG. 2: Blow ups of (a)  $\langle V_x \rangle$  vs  $F_D$  and (b)  $\delta V_x$  (blue) and  $\delta V_y$  (red) vs  $F_D$  near the conduction threshold for the system in Fig. 1 with  $F = 0.4$  and  $F_p = 0.5$ . There are finite jumps both up and down in all three quantities. There are also a number of isolated jumps within the pinned phase that correspond to avalanche motion.

when the channels close or change shape and the flow is reduced. Once a channel has formed, the velocity of the charges in that channel increases with increasing  $F_D$  until there is a sudden rearrangement of charges somewhere in the system that creates a new channel or shuts down one or more of the existing channels. The jump down in  $\langle V_x \rangle$  for increasing  $F_D$  is indicative of negative differential conductivity. For  $F_D \geq 0.34$ , the channels become more chaotic and randomly change over time, causing the overall flow to be more two-dimensional in character.

In Fig. 3(a) we plot  $\langle V_x \rangle$  versus  $F_D$  for the system from Fig. 1 with  $F_p = 0.5$  at different filling factors of  $F = 1.4, 1.0, 0.8, 0.6, 0.4, 0.3, 0.2$ , and  $0.1$ , while Fig. 3(b) shows the corresponding  $\delta V_x$  versus  $F_D$ . As the filling factor, and thus the charge density, increases, the depinning threshold shifts to lower drives, in agreement with experimental observations<sup>37</sup>. The dashed line in Fig. 3(a) indicates the velocity response that would appear in a system with no pinning. The jump in the velocity response at the transition to continuous disordered flow is sharper for lower fillings. There is a peak in  $\delta V_x$  at the onset of the disordered flow regime, followed by a decrease in  $\delta V_x$  with increasing  $F_D$ . The  $\delta V_x$  curves indicate that the filamentary flow highlighted in Fig. 2 only occurs for  $F > 0.3$ .

In Fig. 4(a) we show a closeup of the  $\langle V_x \rangle$  versus  $F_D$  curve for the system in Fig. 3 at  $F = 0.2$ , where a single depinning transition occurs at  $F_D = 0.44$  from a pinned phase to a disordered or plastic flow phase, and there is no filamentary flow. Figure 4(b) shows the same system at  $F = 0.6$ , which depins near  $F_D = 0.19$  into a

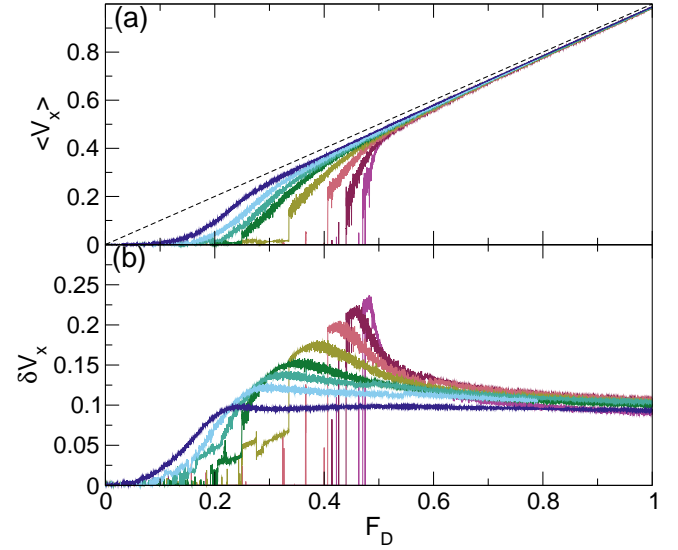


FIG. 3: (a)  $\langle V_x \rangle$  versus  $F_D$  for the system from Fig. 1 with  $F_p = 0.5$  at fillings of  $F = 1.4$  (dark blue), 1.0, 0.8, 0.6, 0.4, 0.3, 0.2, and 0.1 (light magenta), from left to right. The dashed line indicates the velocity response in a sample with no pinning. (b) The corresponding  $\delta V_x$  versus  $F_D$ . The depinning threshold decreases with increasing charge density, and the filamentary phase only occurs for  $F > 0.3$ .

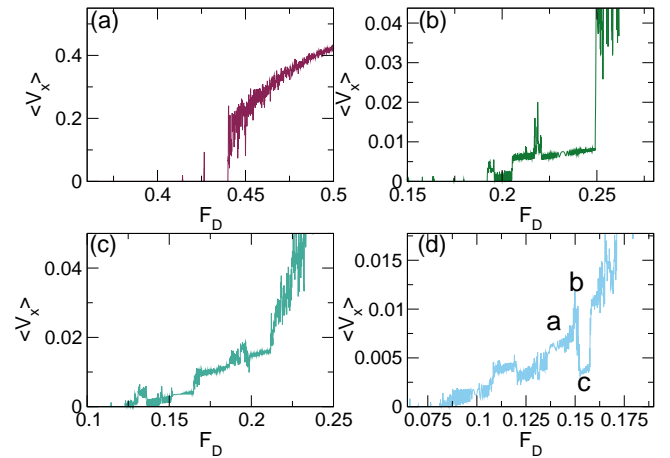


FIG. 4: A blowup of the  $\langle V_x \rangle$  vs  $F_D$  curves for selected samples from Fig. 3 with  $F_p = 0.5$ . (a)  $F = 0.2$  where there is no filamentary regime. (b)  $F = 0.6$  showing a filamentary regime. (c)  $F = 0.8$ . (d)  $F = 1.0$ . The letters a, b, c in panel (d) indicate the values of  $F_D$  at which the images in Fig. 5(a,b,c) were obtained.

filamentary flow phase and then exhibits several upward and downward jumps in the velocity. Immediately after most of these jumps, the velocity increases linearly with  $F_D$  and shows an oscillatory behavior that we discuss in section IV. Near  $F_D = 0.25$  there is a transition to the plastic fluctuating flow phase. In Fig. 4(c), a sample with  $F = 0.8$  has an extended filamentary regime, while in Fig. 4(d), at  $F = 1.0$ , there is a filamentary regime

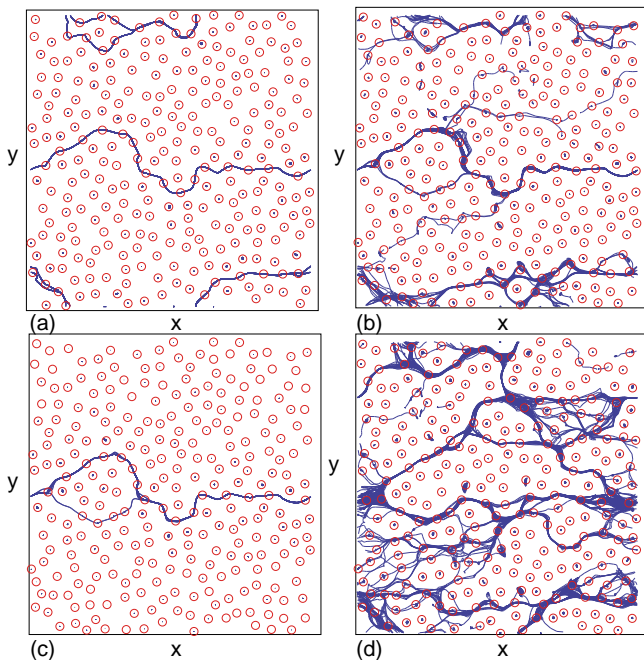


FIG. 5: Images of the charge locations (red circles) and trajectories (lines) for the system in Fig. 4(d) with  $F_p = 0.5$  and  $F = 1.0$ . The letters in Fig. 4(d) correspond to the values of  $F_D$  at which the images were obtained. (a) Stable filamentary channels at  $F_D = 0.137$ . (b) The filamentary regime just after a switching event at  $F_D = 0.15$  where the number of flow channels increases,  $\langle V_x \rangle$  jumps upward, and the channels gradually change over time. (c) The filamentary regime at  $F_D = 0.152$  after a switch in which  $\langle V_x \rangle$  drops and the flow is confined to a single branched channel. (d) Fluctuating channels at  $F_D = 0.2$ .

showing numerous switches corresponding to both positive and negative differential conductivity. As Fig. 4 illustrates, the filamentary flow regime is robust over a range of fillings, and in general the extent of the filamentary flow increases as  $F$  becomes larger.

To get a better picture of the flow in the different phases, in Fig. 5 we show the charge trajectories for the drives labeled with letters in Fig. 4(d). At  $F_D = 0.137$  in Fig. 5(a), there are two q1D winding flow channels or filaments. As  $F_D$  increases, the same channels persist but the flow through each channel becomes faster. At  $F_D = 0.15$ , there is a sudden rearrangement of the charges leading to a jump up in  $\langle V_x \rangle$  since there are now more channels flowing, as illustrated in Fig. 5(b). The channels of Fig. 5(b) slowly change over time, whereas the channel structure in Fig. 5(a) is static. At  $F_D = 0.152$ , there is a transition to the single stable channel state shown in Fig. 5(c), and  $\langle V_x \rangle$  drops below the value it had in Figs. 5(a) and (b) even though  $F_D$  is higher. This channel structure remains stable under increasing  $F_D$  until the next switching event occurs. In some switching events, there is a transition to fluctuating channels, while in other events, a transient fluctuating state settles into a

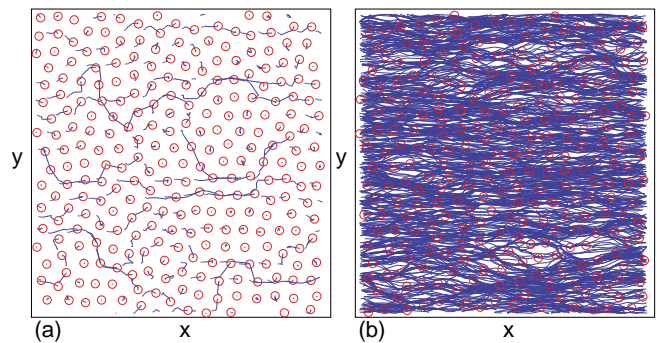


FIG. 6: Images of the charge locations (red circles) and trajectories (lines) for the system in Fig. 4(d) with  $F_p = 0.5$  and  $F = 1.0$  in the disordered regime at  $F_D = 0.3$ . (a) A short time trajectory image shows that the flow is 2D in character and that moving and temporarily pinned charges coexist. (b) A longer time trajectory image indicates that all of the charges participate in the motion over time and the behavior is liquid like.

stable filamentary flow state. The general features found in Fig. 5(a,b,c) also occur for the other jumps in  $\langle V_x \rangle$  in the filamentary flow phase of Fig. 4(d). As  $F_D$  is further increased, the channel structure eventually breaks down and is replaced with a disordered and continuously changing flow, such as that shown in Fig. 5(d) at  $F_D = 0.2$ . At even higher drives, the disordered flow becomes more two-dimensional in character and consists of coexisting moving and temporarily pinned charges, as illustrated in Fig. 6 at  $F_D = 0.3$ . The short time trajectories in Fig. 6(a) show that there is a coexistence of moving and temporarily pinned charges, while the longer time trajectories of Fig. 6(b) indicate that there are no permanently pinned regions and the overall flow is liquid like in nature.

Flow through q1D channels has also been observed for other systems of particles moving over quenched disorder<sup>1</sup>; however, in most of these systems there is not a clearly defined filamentary flow phase. Instead, systems with shorter range interactions show a continuous crossover between filamentary flow and a 2D disordered flow phase. Grønbech-Jensen *et al.*<sup>15</sup> considered a 2D simulation of vortices in thin film superconductors and found a clear region of filamentary flow at lower drives followed by disordered 2D flow at higher drives. The interactions between vortices in thin film superconductors obey a  $\ln(r)$  potential or a  $1/r$  force, in contrast to vortex lines in bulk superconducting crystals, where the interaction is a Bessel function that is similar to a screened Coulomb potential. Grønbech-Jensen *et al.* argued that due to the long range interactions in the thin film system, the shear modulus  $C_{66}$  of the vortex lattice is much lower than the compression modulus, so the vortices can easily slide past each other, favoring filamentary motion. The filamentary flow can also be viewed as a consequence of the existence of interstitial vortices, which occupy the spaces between pinning sites and are immobilized only

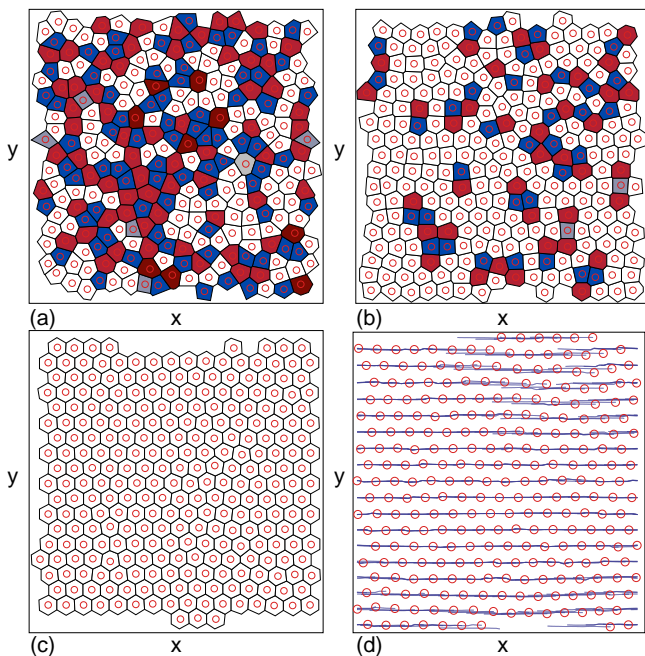


FIG. 7: (a,b,c) Voronoi constructions of the charge locations (red circles) in the system from Fig. 4(d) with  $F_p = 0.5$  and  $F = 1.0$ . Polygon colors indicate the coordination number of each electron: 4 (dark grey), 5 (blue), 6 (white), 7 (light red), 8 (dark red), 9 (light grey). (a)  $F_D = 0.25$ . (b)  $F_D = 0.45$ . (c)  $F_D = 0.8$ . The system becomes more ordered with increasing drive and forms a moving smectic at the highest drive. (d) Image of the charge locations (red circles) and trajectories (lines) for the sample in panel (c) with  $F_D = 0.8$ , showing straight non-crossing channels of flow.

due to the repulsion of neighboring pinned vortices rather than being trapped directly by a pinning site. If the interaction potential between vortices is very smooth, as is the case for a  $\ln(r)$  potential, the potential landscape experienced by an interstitial vortex will be fairly flat. For shorter range interaction potentials, the landscape looks more like a series of obstacles in which the vortices can become trapped. This suggests that for a Wigner crystal with no screening, where the charge-charge interactions are of long range, filamentary flow phases should be a general feature. On the other hand, if screening is occurring, the behavior will be closer to that of bulk superconducting vortices or particles with short range interactions, and the filamentary flow phase will be lost.

At higher drives, the charges dynamically order into a moving crystal or moving smectic state. In general, there are still a small number of lattice defects present, so the system is best described as a weak moving smectic. In Fig. 7(a,b,c) we show Voronoi constructions of the charge positions at  $F_D = 0.25$ ,  $0.45$ , and  $0.8$ , respectively, where polygon colors indicate the coordination number  $z_i$  of each charge. The system is strongly disordered at  $F_D = 0.25$  in Fig. 7(a) and contains numerous topological defects, while at  $F_D = 0.45$  in Fig. 7(b), the number of defects is reduced. In Fig. 7(c) at  $F_D = 0.8$ ,

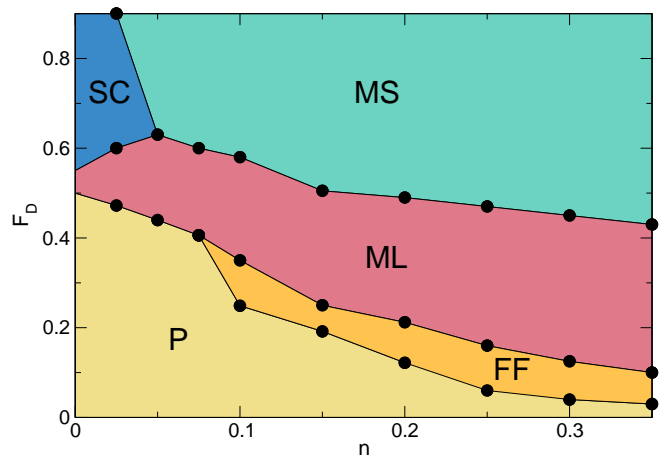


FIG. 8: Dynamic phase diagram as a function of driving force  $F_D$  vs charge density  $n$  for the system in Figs. 4 and 5 with  $F_p = 0.5$ . Since the pinning density is always fixed to  $n_p = 0.25$ , the filling factor  $F = N/N_p = n/n_p = 4n$ . The phases are: P, pinned (yellow); FF, filamentary flow (orange); ML, disordered moving liquid (pink); SC, moving semi-crystallized state (blue); MS, moving smectic (green).

the lattice is almost completely triangular and contains only sixfold coordinated charges. The charge trajectories at  $F_D = 0.8$ , shown in Fig. 7(d), follow straight 1D channels that do not intersect. Dynamical reordering transitions for driven Wigner crystals was studied previously in a system with long range pinning sites<sup>35</sup>. In the present study, the pinning sites are of short range, and the Wigner crystal is able to organize into a state containing almost no topological defects. In contrast, in Ref.<sup>35</sup>, the long range pinning interfered with the dynamical reordering and the system only reached a moving smectic state in which a finite number of topological defects persist that are aligned so as to glide along the driving direction.

From the features in the  $\langle V_x \rangle$ ,  $\delta V_x$ , and  $F_D$  curves, along with the images of the topological defects, we construct a dynamic phase diagram as a function of  $F_D$  versus charge density  $n$  for a system with fixed  $F_p = 0.5$ , as shown in Fig. 8. Since the pinning density is always fixed at  $n_p = 0.25$ , we have  $F = N/N_p = n/n_p = 4n$  and  $n = F/4$ . For  $n < 0.1$ , the system depins directly into a disordered moving liquid phase and the filamentary flow state is absent, as shown in Fig. 4(a). At high drives, a moving smectic forms if the charge density is high enough, and in some cases the system is small enough for this smectic to completely order into a moving crystal without defects. When the charge density is very low, some randomly oriented topological defects remain present even at high drives and the system forms a partially ordered crystal or semi-crystal. For  $n > 0.075$ , a window of filamentary flow phase appears above depinning, as illustrated in Fig. 5(a,b,c), followed by a transition into the fluctuating disordered moving liquid. The filamentary flow phase is lost at low charge densities be-

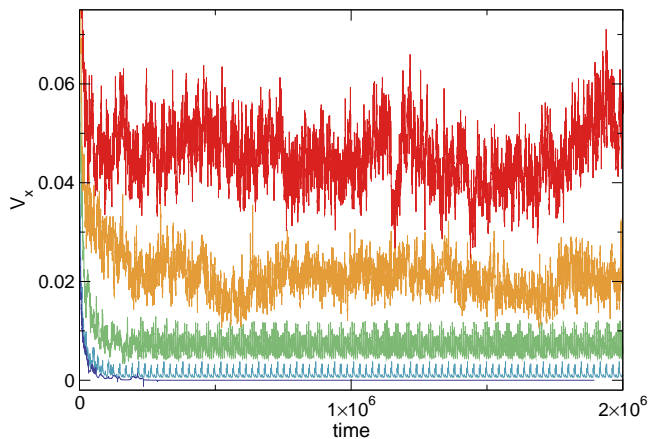


FIG. 9: Time series of the velocity  $V_x$  after application of a pulse drive for a system with  $F = 1.0$  and  $F_p = 0.5$ . At  $F_D = 0.04$  (dark blue), the system reaches a pinned state. For  $F_D = 0.075$  (light blue) and  $F_D = 0.1375$  (green), the system settles into filamentary flow with a periodic velocity signal. For  $F_D = 0.175$  (orange) and  $F_D = 0.2$  (red), the system settles into a fluctuating state.

cause all of the charges are able to occupy strong pinning sites and there are no interstitial charges. The depinning threshold marking the end of the pinned phase drops to lower  $F_D$  with increasing  $n$ , in agreement with recent experiments<sup>37</sup>.

#### IV. NOISE MEASURES

We next consider the system from Fig. 4(d) with  $F_p = 0.5$  and  $F = 1.0$  but for a pulsed drive, where we apply a fixed  $F_D$  and wait for the system to settle into a steady state before measuring the noise fluctuations and obtaining the long time average velocity. In Fig. 9 we plot  $V_x$  versus time in simulation time steps for pulse drive amplitudes of  $F_D = 0.04, 0.075, 0.1375, 0.175$ , and  $0.2$ . For  $F_D = 0.04$ , there is some initial transient motion, but at longer times all of the charges become pinned and the velocity drops to zero. At  $F_D = 0.075$  and  $F_D = 0.1375$ , after an initial decreasing transient, the velocities settle into a periodic pattern reflecting the formation of a filamentary flow state containing one or more flow channels of repetitive motion. Unlike the simulations of section III in which the drive is continuously increasing, for the pulsed drive the filamentary channels adopt a stable configuration and there is no switching. In general, for the filamentary flow the system settles into a state with a periodic velocity signal. The periodicity of the signal can be fairly complicated if there are multiple filaments of flow present that generate multiple frequencies simultaneously. For  $F_D = 0.175$  and  $F_D = 0.2$ , there is still an initial transient decay of the velocity but the system remains in a fluctuating state at long times.

By performing a series of pulse measurements, we

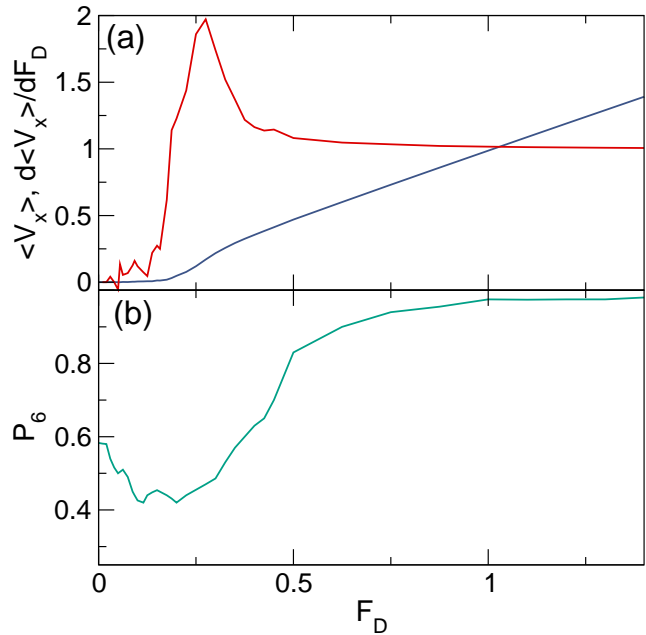


FIG. 10: (a) The average velocity  $\langle V_x \rangle$  (blue) and its derivative  $d\langle V_x \rangle/dF_D$  (red) vs  $F_D$  for the system in Fig. 9 with  $F = 1.0$ ,  $F_p = 0.5$ , and pulse driving, showing a two step depinning process. (b) The corresponding average fraction of sixfold coordinated charges  $P_6$  vs  $F_D$ . The system is the most disordered in the fluctuating phase and undergoes a dynamical reordering transition at higher  $F_D$ .

obtain the average velocity  $\langle V_x \rangle$  and its derivative  $d\langle V_x \rangle/dF_D$  as a function of  $F_D$ , as plotted in Fig. 10(a) for the system in Fig. 9. The initial depinning into a filamentary flow state occurs near  $F_D = 0.0625$ , and the filamentary flow, which extends from  $0.0625 \leq F_D < 0.175$ , produces a series of small jumps in  $d\langle V_x \rangle/dF_D$ . For  $0.175 \leq F_D < 0.5$ , the system enters a disordered strongly fluctuating flow phase associated with a large peak in  $d\langle V_x \rangle/dF_D$ , while for  $F_D \geq 0.5$ , the velocity increases linearly with  $F_D$  and  $d\langle V_x \rangle/dF_D$  approaches one. The behavior of the velocity-force curve is similar to recent experimental observations of nonlinear velocity-force signatures showing a two step depinning process into a nonlinear regime at the onset of conduction followed by a transition to a linear regime at higher drives<sup>37</sup>. We show in section V that as the strength  $F_p$  of the disorder increases, the multiple step depinning transitions become even more prominent. Figure 10(b) illustrates the fraction of the average number of sixfold coordinated particles,  $P_6 = N^{-1} \sum_i \delta(z_i - 6)$ , versus  $F_D$ . A local dip in  $P_6$  occurs at the transition from filamentary flow to fluctuating flow, and there is a large increase in  $P_6$  near  $F_D = 0.5$  when the system transitions from the plastic disordered flow state to a moving smectic.

The different phases produce signatures in the velocity noise power spectra  $S(f)$ , obtained from the time series of the conduction fluctuations shown in Fig. 9 according

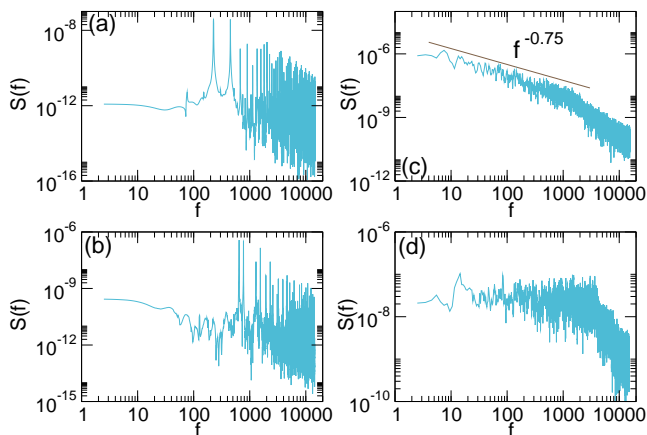


FIG. 11: Velocity noise power spectra  $S(f)$  for the pulse drive system from Figs. 9 and 10 with  $F = 1.0$  and  $F_p = 0.5$ . (a) At  $F_D = 0.075$ , for the filamentary flow shown in Fig. 9, there is a narrow band noise signal. (b) At  $F_D = 0.1375$ , a filamentary flow phase at a higher drive also shows narrow band noise. (c) At  $F_D = 0.25$ , in the fluctuating regime, for low frequencies we find  $S(f) \propto 1/f^\alpha$  with  $\alpha = 0.75$ . (d) At  $F_D = 0.35$ , the low frequency noise power is reduced.

to

$$S(f) = \frac{1}{2\pi} \left| \int V(t) e^{-i2\pi ft} dt \right|^2. \quad (2)$$

In computing the power spectrum, we discard the transient portion of the velocity time series and only consider the time period during which the system has reached a steady state. In Fig. 11(a) we plot  $S(f)$  for the filamentary flow phase at  $F_D = 0.075$  from Fig. 9. Here we find a narrow band signal with multiple peaks produced by the periodicity of the flow of charges through the q1D channels. At  $F_D = 0.1375$  in Fig. 11(b), a filamentary flow state at higher drives has narrow band peaks that are shifted to higher frequency since the charges are moving more rapidly through the flow channels. The power spectrum becomes more complicated as additional channels of flow open, giving multiple different frequencies of flow. In Fig. 11(c) we plot  $S(f)$  in the fluctuating liquid regime at  $F_D = 0.25$ . The peaks associated with the periodic filamentary flow channels are lost and the noise power at low frequencies assumes a  $1/f^\alpha$  form, where the solid line is a fit with  $\alpha = 0.75$ . This is close to the exponent values obtained in recent noise measures on sliding Wigner crystals, where  $\alpha = 0.6$ <sup>37</sup>. As the drive increases further, the low frequency noise power is reduced and the spectrum at low frequencies becomes white, as shown in Fig. 11(d) for  $F_D = 0.35$ . When the moving smectic state forms for even higher drives, new narrow band noise peaks emerge that are associated with the washboard frequency. Washboard noise signals for moving crystals or moving smectics at higher drives have been studied in both simulation and experiment for sliding charge density waves<sup>17</sup>, superconducting

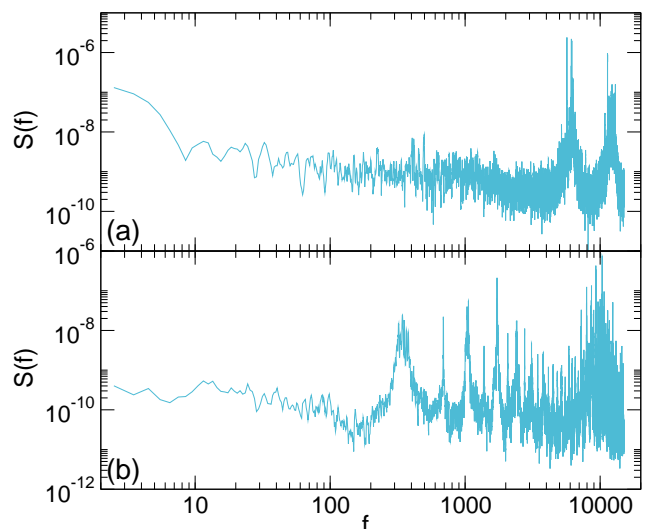


FIG. 12:  $S(f)$  for the system from Figs. 9 and 10 with  $F = 1.0$  and  $F_p = 0.5$ . (a)  $F_D = 0.55$  in the moving smectic phase, showing a narrow band signal at higher frequencies. (b)  $F_D = 1.0$ , where there is a pronounced low frequency washboard signal.

vortices<sup>16,24,78,79</sup>, and magnetic skyrmions<sup>26,27,80</sup>, and have been predicted to occur for Wigner crystals<sup>33</sup>. Simulations of Wigner crystals moving over long range disorder also produced a washboard signal<sup>35</sup>; however, in the previous work the narrow band noise in the filamentary flow regime was not studied<sup>35</sup>.

In Fig. 12(a) we plot  $S(f)$  for the system in Fig. 10 at  $F_D = 0.55$ . A narrow band noise signal has emerged since the system is transitioning into a moving smectic with a small number of topological defects. At  $F_D = 1.0$  in Fig. 12(b), the ordering of the charge lattice has increased and there is a stronger narrow band noise signal along with a washboard signal at lower frequencies.

In Fig. 13 we plot  $S_0$ , the noise power at a low fixed frequency of  $f_0 = 20$ , versus  $F_D$  for the  $F = 1.0$  and  $F_p = 0.5$  system. The noise power is low in the filamentary flow phase, high in the fluctuating moving liquid, and low in the dynamically reordered moving smectic phase. There is a peak in  $S_0$  near  $F_D = 0.25$ . This falls within the range  $0.175 \leq F_D < 0.3$  in which the noise develops  $1/f^\alpha$  characteristics, as shown in Fig. 11(c). The noise is white at higher drives of  $0.3 \leq F_D < 0.5$ , similar to what is shown in Fig. 11(d). For  $0.5 < F_D < 0.8$ , a narrow band noise signal similar to that in Fig. 12(a) appears, while for  $F_D \geq 0.8$ , even fewer topological defects are present in the lattice and the noise peaks sharpen, as shown in Fig. 12(b). The peak in the noise power illustrated in Fig. 13 is similar to low temperature experimental results<sup>37</sup> in which the noise power is small at low drives, reaches a strong peak near depinning, and drops again at higher drives.

The appearance of low frequency narrow band noise near depinning and broad band noise at higher drives



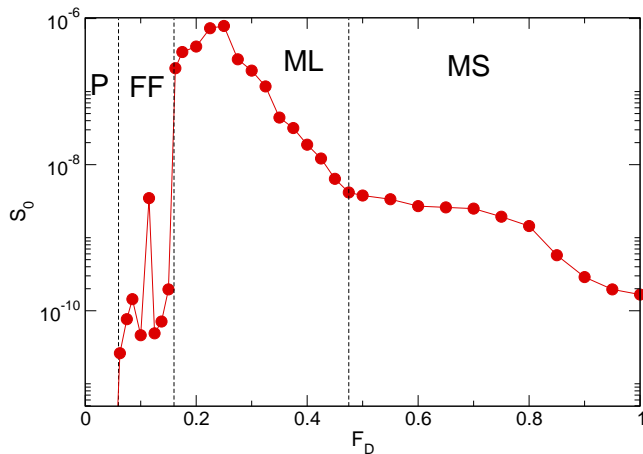


FIG. 13: The noise power  $S_0$  at a low fixed frequency of  $f_0 = 20$  vs  $F_D$  for the system from Figs. 9 and 10 with  $F = 1.0$  and  $F_p = 0.5$ .  $S_0$  is zero in the pinned (P) phase, low in the filamentary flow (FF) phase, has a peak in the disordered moving liquid (ML) phase, and drops again in the ordered moving smectic (MS) phase.

has also been observed for Wigner crystals and electron liquid crystals<sup>20,28</sup>. In the work of Sun *et al.*<sup>28</sup>, transitions among ordered and disordered phases occur as a function of drive, and the ordered phases exhibit narrow band noise features. This could indicate that there are regimes of stable filament flow interspersed with fluctuating flow regimes, and that at high drives the system dynamically reorders. In our case, in the filamentary flow regime the system generally jumps from one ordered state to another, but there are situations in which the charges remain in a fluctuating state between the stable filamentary regimes. This occurs more frequently for continuous driving, as shown in Fig. 4(c). If temperature is added, additional fluctuating flow phases might emerge. The narrow band noise in the filamentary phase does not arise from the presence of strong ordering, for the filamentary phase is structurally disordered. Instead, since the q1D filaments are stable, motion along the filaments repeats very reliably as a function of time. One question is whether the fluctuating regimes are transient, meaning that the system might order after a sufficiently long time interval, or whether they are in fact stable, meaning that it is only possible for the system to reach an ordered state for higher drives. In systems where charged stripes or bubbles can arise, such as in reentrant quantum Hall systems, experimental measurements show that there is narrow band noise<sup>81</sup>. In experiments on 2D electron systems, nonlinear current-voltage curves interpreted as signatures of the depinning of electron nematics or smectics are also associated with  $1/f$  noise<sup>21</sup>.

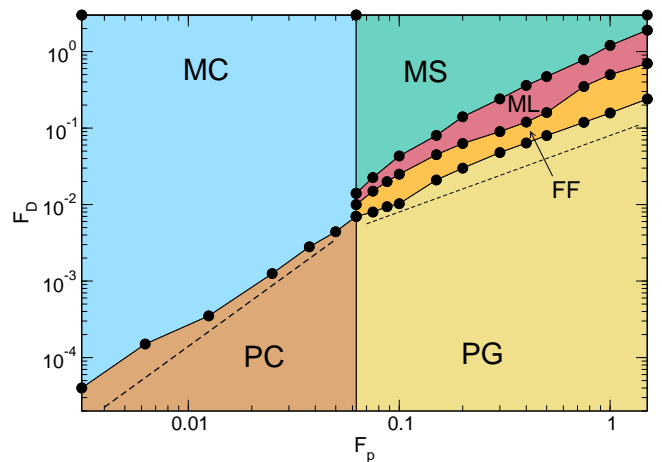


FIG. 14: Dynamic phase diagram as a function of  $F_D$  vs pinning strength  $F_p$  for a system with  $F = 1.0$ . At low  $F_p$ , there is a pinned crystal (PC, light brown) that depins elastically into a moving crystal (MC, light blue). For higher  $F_p$ , the system is initially in a pinned glass state (PG, yellow) that depins plastically into the filamentary flow regime (FF, orange). At higher drives, there is a transition to the disordered moving liquid (ML, pink) state and a reordering into the moving smectic (MS, green) state. Fits to the depinning curve are shown as dashed lines: left,  $F_c \propto F_p^2$ ; right,  $F_c \propto F_p$ .

## V. VARIED DISORDER STRENGTH

We next consider the effects of changing the pinning strength  $F_p$ . We first focus on a system with fixed  $F = 1.0$  and measure the velocity-force curves and  $P_6$  versus  $F_D$ . From this data, we construct the dynamic phase diagram as a function of  $F_D$  versus  $F_p$  plotted in Fig. 14. For  $F_p \geq 0.075$ , the ground state at  $F_D = 0.0$  is a disordered pinned glass since the pinning is strong enough to induce the formation of topological defects in the Wigner crystal. This pinned glass depins into the filamentary flow phase, which exhibits narrow band noise. At higher drives, there is a transition into the fluctuating moving liquid phase with  $1/f$  noise, followed by dynamical reordering into a moving smectic. The depinning threshold for the pinned glass increases linearly with  $F_p$ , as indicated by the dashed line showing a fit to  $F_c \propto F_p$ , similar to what has been observed in previous work on plastic depinning transitions<sup>1</sup>. The drives at which the system transitions from the filamentary flow phase to the disordered moving liquid and from the moving liquid to the moving smectic also increase linearly with increasing  $F_p$ . For  $F_p < 0.075$ , the disorder is weak enough that no topological defects form in the pinned state, and a pinned crystal appears that depins elastically to a moving crystal. In this regime, the filamentary flow and disordered moving liquid phases are absent. In general, when the pinning is strong, some topological defects form in the moving state, and since these defects align so as to glide in the driving direction, the system is best described as a moving smectic. In contrast, when the disorder is weak,

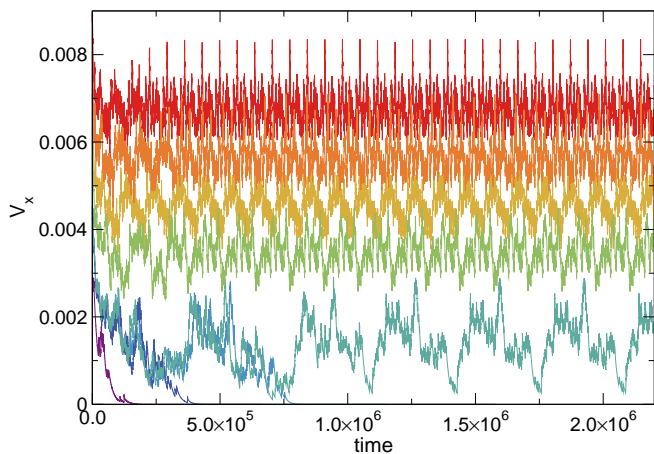


FIG. 15: Time series of the velocity  $V_x$  in the elastic depinning regime for the system in Fig. 14 with  $F = 1.0$  at  $F_p = 0.05$  and  $F_D = 0.0035$  (violet),  $0.00425$  (dark blue),  $0.00435$  (light blue),  $0.0044$  (teal),  $0.006$  (green),  $0.007$  (yellow),  $0.008$  (orange), and  $0.009$  (red). For  $F_D < 0.044$  the system evolves to a pinned state. For  $F_D \geq 0.044$ ,  $V_x$  develops a washboard or periodic noise signal.

there are no topological defects and the system is described as a moving crystal. The depinning threshold in the elastic depinning regime obeys  $F_c \propto F_p^2$ , as expected for collective or elastic depinning<sup>1</sup>.

In the elastic depinning regime, there is no filamentary flow and the depinning occurs in a single step, giving transport and noise signatures that are very distinct from those found for the plastic depinning transition where filamentary flow occurs. In Fig. 15 we plot the velocity time series  $V_x$  for the system in Fig. 14 at  $F_p = 0.05$  over a range of  $F_D$  from  $F_D = 0.0035$  to  $F_D = 0.009$  that spans the depinning threshold. For  $F_p < 0.044$ , the flow is transient and the system settles into a pinned state. For  $F_D \geq 0.044$ , the motion persists and develops a complex periodic signal. As  $F_D$  increases, the magnitude of  $V_x$  and the frequency of its oscillations both increase. This result indicates that in the elastic depinning regime, a washboard signal emerges above the depinning threshold.

Figure 16(a) shows  $\langle V_x \rangle$  versus  $F_D$  for the system in Fig. 15, where the dashed line is the pin free response. The corresponding  $d\langle V_x \rangle/dF_D$  versus  $F_D$  in Fig. 16(b) has a single sharp peak at depinning, in contrast to the double peak that appears in a two step plastic depinning process. When the depinning is elastic, both the filamentary flow phase and switching events are absent. In Fig. 17(a,b,c) we plot the Fourier transform  $\hat{V}(f)$  of the velocity time series  $V_x$  for the system in Fig. 15 at  $F_D = 0.9$ ,  $0.7$ , and  $0.044$ , respectively. The narrow band noise peaks shift to higher frequencies as  $F_D$  increases.

For larger  $F_p$ , the velocity-force curves exhibit stronger cusps at the transitions among the different phases. Recent experimental work identified a regime in which there is a clear two step depinning process, with an initial transition to a nonlinear regime followed by a second tran-

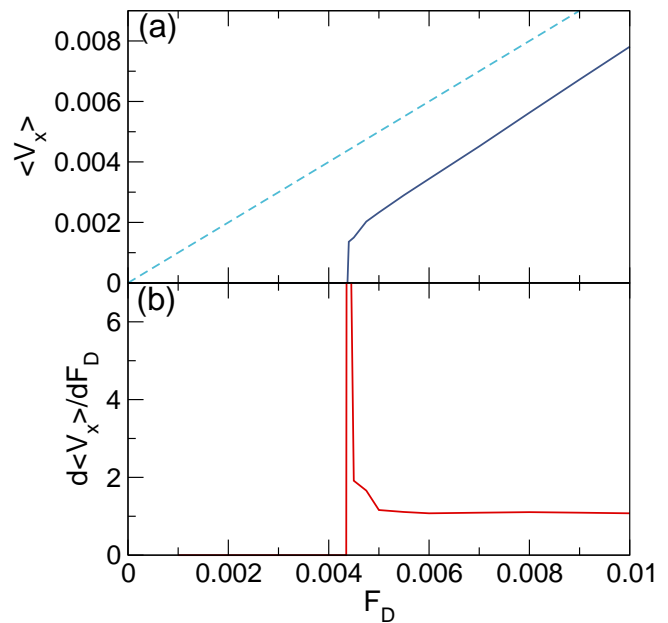


FIG. 16: The average velocity  $\langle V_x \rangle$  (solid line) vs  $F_D$  for  $F_p = 0.05$  in the elastic depinning regime of the system from Fig. 14 and Fig. 15 with  $F = 1.0$ . The dashed line is the pin free result. (b) The corresponding  $d\langle V_x \rangle/dF_D$  versus  $F_D$  has a single sharp peak at depinning.

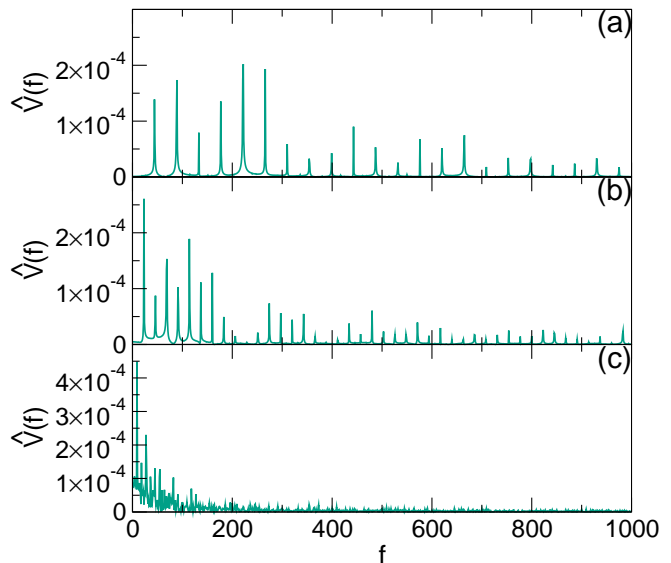


FIG. 17: The Fourier transform  $\hat{V}(f)$  of the velocity time series  $V_x$  for the system in Fig. 15 with  $F = 1.0$  and  $F_p = 0.05$  at  $F_D =$  (a)  $0.9$ , (b)  $0.7$ , and (c)  $0.044$ . The narrow band noise peaks shift to higher frequencies with increasing  $F_D$ .

sition to a phase in which the velocity increases linearly with increasing drive<sup>37</sup>. In Fig. 18 we plot  $\langle V_x \rangle$  versus  $F_D$  for a system with  $F_p = 1.5$  and  $F = 0.4$ . To obtain this curve, we increase the driving force in increments of  $\Delta F_D = 0.004$  and spend 888400 simulation time steps on each increment in order to obtain an average velocity

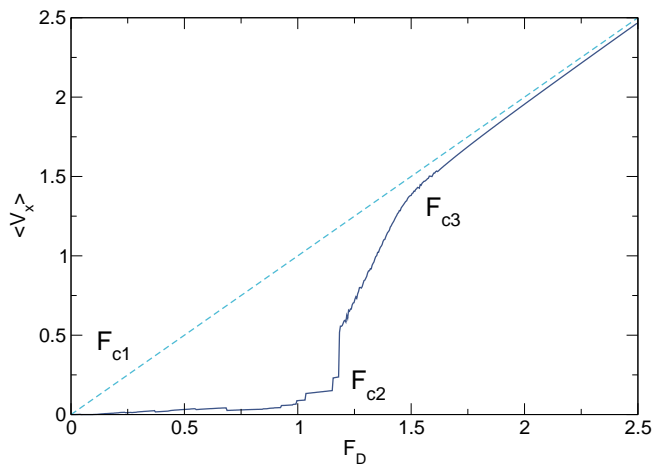


FIG. 18:  $\langle V_x \rangle$  vs  $F_D$  for a system with  $F_p = 1.5$  and  $F = 0.4$ . The drive is increased in increments of  $\Delta F_D = 0.004$  and we spend 888400 simulation time steps at each increment to obtain the average velocity value.  $F_{c1}$  is the transition from pinned to filamentary flow,  $F_{c2}$  denotes the transition from filamentary to disordered fluctuating flow, and  $F_{c3}$  is the transition from disordered to linear flow.

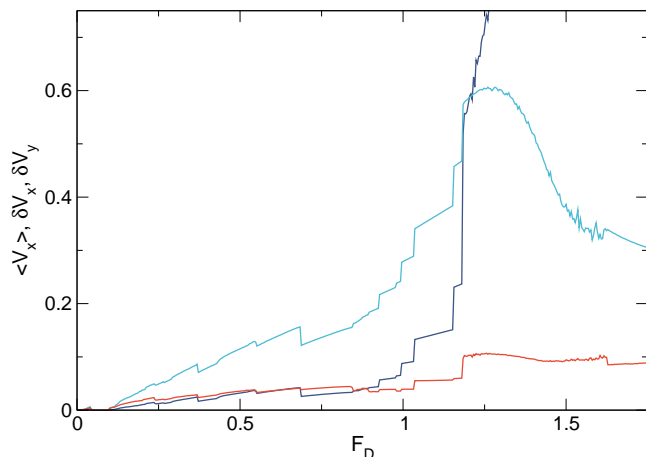


FIG. 19:  $\langle V_x \rangle$  (dark blue),  $\delta V_x$  (light blue), and  $\delta V_y$  (red) vs  $F_D$  from the filamentary regime through the transition to the plastic flow regime for the system in Fig. 18 with  $F_p = 1.5$  and  $F = 0.4$ .

and produce a smoother velocity-force curve. As Fig. 18 shows, there is an extended regime of filamentary flow. The transition from the pinned state to the filamentary flow state is labeled  $F_{c1}$ , the transition from filamentary flow to the disordered fluctuating flow state is marked  $F_{c2}$ , and the transition to the linear flow state is denoted  $F_{c3}$ . In the experimental work of Ref.<sup>37</sup>, only  $F_{c2}$  and  $F_{c3}$  were observed. It may be possible that there is a filamentary flow phase that is not resolvable experimentally due to the large fluctuations in the data. In Fig. 19 we plot  $\langle V_x \rangle$ ,  $\delta V_x$ , and  $\delta V_y$  versus  $F_D$  from the filamentary regime through the transition to plastic flow regime. Within the filamentary regime, a series of upward and downward

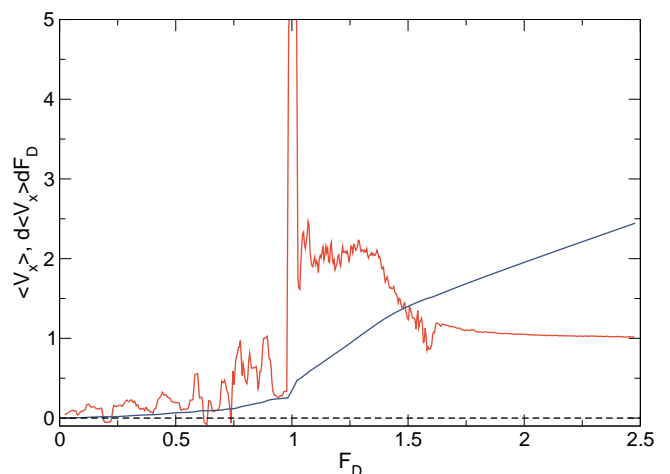


FIG. 20:  $\langle V_x \rangle$  (blue) and  $d\langle V_x \rangle/dF_D$  (red) vs  $F_D$  for a system with  $F_p = 1.5$  and  $F = 0.8$ . The dashed line indicates that  $d\langle V_x \rangle/dF_D$  makes excursions below zero.

jumps occur in  $\langle V_x \rangle$  corresponding to the opening and closing of individual flow channels. These jumps are also correlated with jumps in  $\delta V_x$  and  $\delta V_y$ . In general,  $\delta V_x$  is larger than  $\delta V_y$ , and a large peak in  $\delta V_x$  appears at the transition to the plastic flow regime.

As we vary the filling at  $F_p = 1.5$ , we find similar velocity-force and velocity fluctuation curves. For example, in Fig. 20 we plot  $\langle V_x \rangle$  and  $d\langle V_x \rangle/dF_D$  versus  $F_D$  for a system with  $F = 0.8$ . The filamentary flow phase is visible as a region of positive and negative peaks in  $d\langle V_x \rangle/dF_D$ . The transition to the nonlinear flow regime is accompanied by a large peak in  $d\langle V_x \rangle/dF_D$ , followed by small dip after which  $d\langle V_x \rangle/dF_D$  approaches 1.0. These results suggest that the two step depinning process observed in Ref.<sup>37</sup> is likely associated with a stronger pinning regime.

## VI. AVALANCHES

As noted in Fig. 1, there are clear jumps in  $\delta V_x$  and  $\delta V_y$  for increasing  $F_D$  within the pinned regime that are associated with charge avalanches. In general, the avalanches are the most prominent in parameter windows where filamentary flow can occur. In Fig. 21 we plot  $V_x$  averaged over a very short time interval versus  $F_D$  for a system with  $F = 0.4$  and  $F_p = 0.5$ . The inset shows an image of one of the avalanches in which the motion occurs along a q1D chain. This motion resembles what is found in the filamentary flow phase, but the duration of the motion is finite, indicating that the avalanches can be viewed as q1D excitations. To obtain better statistics on the avalanche behavior, we performed a series of 100 different disorder realizations with different pinning site locations and swept the value of  $F_D$  as in Fig. 21. We define the size  $s$  of the avalanche to be the magnitude of  $V_x$ . In Fig. 22 we plot the avalanche size distribution  $P(s)$  on a log-

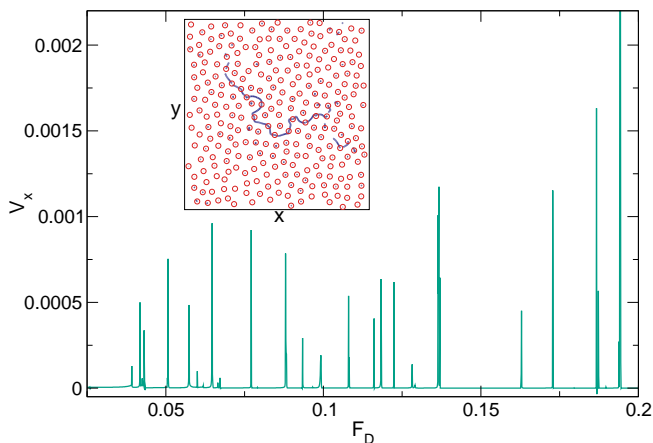


FIG. 21:  $V_x$  averaged over a very short time interval vs  $F_D$  for a system with  $F = 0.4$  and  $F_p = 0.5$  in the pinned regime showing a series of avalanches. Inset: Image of the electron locations (red circles) and trajectories (lines) showing an example of an avalanche in which the motion occurs along a q1D chain.

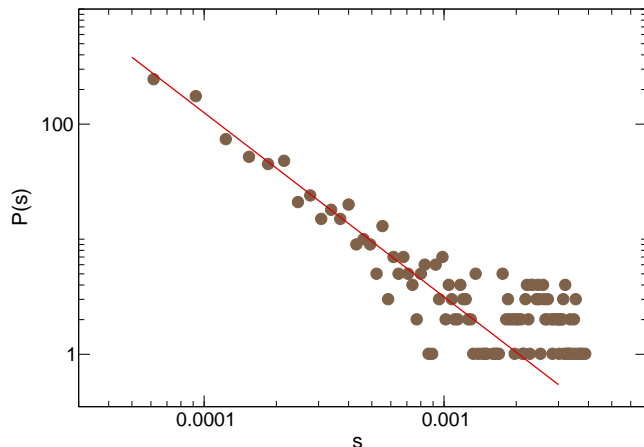


FIG. 22: Distribution  $P(s)$  of the avalanche sizes measured in terms of the magnitude of  $V_x$  during the avalanche event for 100 disorder realizations of the system from Fig. 20 with  $F = 0.4$  and  $F_p = 0.5$  in the pinned regime. The dashed line is a power law fit to  $P(s) \propto s^{-\tau}$  with  $\tau = 1.6$ .

log scale. The behavior is consistent with  $P(s) \propto s^{-\tau}$ , where the solid line is a fit with  $\tau = 1.6$ . Previous work on avalanches in three dimensional Coulomb systems obtained an avalanche exponent of  $\tau = 1.5$ <sup>82</sup>. Among systems of particles moving over random pinning, the one with q1D avalanches that is the closest to what we observe here is vortices in type II superconductors, where avalanches in the strong pinning regime form q1D like chains and the avalanche sizes are power law distributed with exponents ranging from  $\tau = 2.0$  to  $\tau = 1.6$ <sup>83,84</sup>. In a magnetic skyrmion system, avalanches were observed with an exponent of  $\tau = 1.5$ <sup>85</sup>. These results indicate that the behavior of charges moving over random dis-

order is similar to that of superconducting vortices and magnetic skyrmions. This is reasonable since all of these systems consist of an assembly of driven particles moving over quenched disorder. In the case of the Wigner crystal, the interactions are Coulomb in form, while for superconducting vortices and magnetic skyrmions, the interactions are closer to screened Coulomb.

For lower values of  $F$ , the avalanches do not occur along q1D chains but rather consist of single hops, and the avalanche distributions show a characteristic peak associated with the velocity of a single electron jumping from one pinning site to the next. Avalanches also occur below depinning in the elastic depinning regime, but these avalanches are 2D in nature and the statistics are much more difficult to obtain. Avalanches in charge ordering systems have been studied in the presence of strong pinning, and the largest number of avalanches occur near what are believed to be critical points as a function of temperature<sup>86</sup>. Future directions include testing whether the avalanche shapes show scaling, as found in crackling noise systems<sup>85,87</sup>.

## VII. DISCUSSION

In the experimental work of Ref.<sup>37</sup>, the current-voltage curves become much more rounded with increasing temperature. This can be interpreted as resulting from an increase in thermal creep. Increasing the temperature also destroyed the peak in the noise power at depinning and led to an overall reduction in the noise power. Future work could examine such thermal effects in greater detail. For example, in the filamentary flow regime, the transport could develop additional thermal switching effects in which thermally induced random hops could cause some channels to open or close even at a fixed drive, giving rise to telegraph noise. It would also be interesting to determine whether the strong narrow band noise signals in the filamentary or moving crystal phases are robust against thermal fluctuations.

In our system, the filamentary flow channels are one particle wide and are essentially one dimensional. Other flow morphologies are possible, such as large scale mesoscopic rivers in which there is a mixture of fluid and solid states, so that large rivers wind through the sample between pinned islands. This type of flow could arise if large scale heterogeneities are present, causing the disorder strength to vary over length scales that are multiple lattice constants of the periodicity of the Wigner crystal. Much larger scale simulations would be needed to explore such regimes, which could include tens to hundreds of thousands of charges.

Another question is the role of screening, which could modify the electron-electron interactions. If screening is important, the interactions would be better described as Yukawa or screened Coulomb in form,  $\exp(-\kappa r)/r$ . Interactions of this type could produce behavior more similar to that of colloidal assemblies moving over random dis-

order, where plastic to elastic depinning transitions have been studied<sup>3,4</sup>. Other directions would be to explore critical behaviors in the velocity scaling or transient effects near the Wigner crystal depinning transition, and compare these to the scaling found in other systems, such as superconducting vortices<sup>88,89</sup>.

### VIII. SUMMARY

We have investigated the nonlinear dynamics of Wigner crystals driven over random disorder by measuring the velocity-force curves, the standard deviation of the velocities, and the fraction of six-fold coordinated charges. For strong disorder, the system forms a pinned Wigner glass that can depin into a filamentary flow state where the motion occurs in well defined quasi-one-dimensional channels. As the drive increases, these channels can open or close, leading to switching events that have either positive or negative differential conductivity. In regimes where there is stable filamentary flow, the noise has a narrow band character, and at the transition to fluctuating filaments or disordered liquid flow, the noise becomes broad band and the noise power at low frequencies grows large. At higher drives, the system enters a continuously fluctuating state in which pinned and mobile electrons coexist and there is a rapid exchange between the two. In this case there is strong broad band noise of  $1/f^\alpha$  form with  $\alpha = 0.7$ . At even higher drives, the system can reorder into a moving smectic where most of the charges have six neighbors and the noise shows a washboard signal. This indicates that for increasing drive, there is a regime of narrow band noise for the initial flow, followed by  $1/f$  noise and a peak of the noise

power in the intermediate plastic flow regime, and then a reappearance of narrow band noise at high drives. For weak quenched disorder, the system forms a pinned crystal that undergoes a single depinning transition into a moving crystal with a strong narrow band noise signal. Within the strong pinning regime, there can be a two or three step depinning process, where there is enhanced filamentary flow with regions of negative differential conductivity, a disordered flow regime, and finally a transition to a regime in which the velocity increases linearly with drive. These phases produce clear signatures in the differential conductivity curves. Many of the transport features we observe are in agreement with recent transport studies on Wigner crystals in a regime where stripes or bubble like charge ordered phases could be occurring. Finally, we find that below the conduction threshold, as the drive is increased there can be large scale rearrangements within the pinned phase in the form of avalanches. These avalanches have quasi-one-dimensional characteristics and their sizes are power law distributed with an exponent of  $\tau = 1.6$ , similar to what is found for avalanches in driven vortices in type-II superconductors.

### Acknowledgments

We gratefully acknowledge the support of the U.S. Department of Energy through the LANL/LDRD program for this work. This work was supported by the US Department of Energy through the Los Alamos National Laboratory. Los Alamos National Laboratory is operated by Triad National Security, LLC, for the National Nuclear Security Administration of the U. S. Department of Energy (Contract No. 892333218NCA000001).

- 
- <sup>1</sup> C. Reichhardt and C. J. O. Reichhardt, Rep. Prog. Phys. **80**, 026501 (2017).
  - <sup>2</sup> S. Bhattacharya and M. J. Higgins, Phys. Rev. Lett. **70**, 2617 (1993).
  - <sup>3</sup> C. Reichhardt and C. J. Olson, Phys. Rev. Lett. **89**, 078301 (2002).
  - <sup>4</sup> A. Pertsinidis and X. S. Ling, Phys. Rev. Lett. **100**, 028303 (2008).
  - <sup>5</sup> A. Vanossi, N. Manini, M. Urbakh, S. Zapperi, and E. Tosatti, Rev. Mod. Phys. **85**, 529 (2013).
  - <sup>6</sup> C. Reichhardt, D. Ray, and C. J. O. Reichhardt, Phys. Rev. Lett. **114**, 217202 (2015).
  - <sup>7</sup> W. Jiang, X. Zhang, G. Yu, W. Zhang, X. Wang, M. B. Jungfleisch, J. E. Pearson, X. Cheng, O. Heinonen, K. L. Wang, et al., Nature Phys. **13**, 162 (2017).
  - <sup>8</sup> C. Sándor, A. Libál, C. Reichhardt, and C. J. Olson Reichhardt, Phys. Rev. E **95**, 032606 (2017).
  - <sup>9</sup> A. Morin, N. Desreumaux, J.-B. Caussin, and D. Bartolo, Nature Phys. **13**, 63 (2017).
  - <sup>10</sup> T. Giamarchi and P. Le Doussal, Phys. Rev. Lett. **76**, 3408 (1996).
  - <sup>11</sup> L. Balents, M. C. Marchetti, and L. Radzihovsky, Phys. Rev. B **57**, 7705 (1998).
  - <sup>12</sup> C. J. Olson, C. Reichhardt, and F. Nori, Phys. Rev. Lett. **81**, 3757 (1998).
  - <sup>13</sup> D. S. Fisher, Phys. Rep. **301**, 113 (1998).
  - <sup>14</sup> Y. Fily, E. Olive, N. Di Scala, and J. C. Soret, Phys. Rev. B **82**, 134519 (2010).
  - <sup>15</sup> N. Grønbech-Jensen, A. R. Bishop, and D. Domínguez, Phys. Rev. Lett. **76**, 2985 (1996).
  - <sup>16</sup> C. Reichhardt, C. J. Olson, and F. Nori, Phys. Rev. B **58**, 6534 (1998).
  - <sup>17</sup> G. Grüner, Rev. Mod. Phys. **60**, 1129 (1988).
  - <sup>18</sup> R. Besseling, P. H. Kes, T. Drose, and V. M. Vinokur, New J. Phys. **7**, 71 (2005).
  - <sup>19</sup> B. Bag, G. Shaw, S. S. Banerjee, S. Majumdar, A. K. Sood, and A. K. Grover, Sci. Rep. **7**, 5531 (2017).
  - <sup>20</sup> K. B. Cooper, J. P. Eisenstein, L. N. Pfeiffer, and K. W. West, Phys. Rev. Lett. **90**, 226803 (2003).
  - <sup>21</sup> Q. Qian, J. Nakamura, S. Fallahi, G. C. Gardner, and M. J. Manfra, Nature Commun. **8**, 1536 (2017).
  - <sup>22</sup> A. C. Marley, M. J. Higgins, and S. Bhattacharya, Phys. Rev. Lett. **74**, 3029 (1995).
  - <sup>23</sup> A. B. Kolton, D. Domínguez, and N. Grønbech-Jensen,

- Phys. Rev. Lett. **83**, 3061 (1999).
- <sup>24</sup> Y. Togawa, R. Abiru, K. Iwaya, H. Kitano, and A. Maeda, Phys. Rev. Lett. **85**, 3716 (2000).
- <sup>25</sup> S. Okuma, J. Inoue, and N. Kokubo, Phys. Rev. B **76**, 172503 (2007).
- <sup>26</sup> S. A. Díaz, C. J. O. Reichhardt, D. P. Arovas, A. Saxena, and C. Reichhardt, Phys. Rev. B **96**, 085106 (2017).
- <sup>27</sup> T. Sato, W. Koshibae, A. Kikkawa, T. Yokouchi, H. Oike, Y. Taguchi, N. Nagaosa, Y. Tokura, and F. Kagawa, Phys. Rev. B **100**, 094410 (2019).
- <sup>28</sup> J. Sun, J. Niu, Y. Li, Y. Liu, L. N. Pfeiffer, K. W. West, P. Wang, and X. Lin, Fund. Res. **2**, 178 (2022).
- <sup>29</sup> E. Y. Andrei, G. Deville, D. C. Glatli, F. I. B. Williams, E. Paris, and B. Etienne, Phys. Rev. Lett. **60**, 2765 (1988).
- <sup>30</sup> V. J. Goldman, M. Santos, M. Shayegan, and J. E. Cunningham, Phys. Rev. Lett. **65**, 2189 (1990).
- <sup>31</sup> F. I. B. Williams, P. A. Wright, R. G. Clark, E. Y. Andrei, G. Deville, D. C. Glatli, O. Probst, B. Etienne, C. Dorin, C. T. Foxon, et al., Phys. Rev. Lett. **66**, 3285 (1991).
- <sup>32</sup> H. W. Jiang, H. L. Stormer, D. C. Tsui, L. N. Pfeiffer, and K. W. West, Phys. Rev. B **44**, 8107 (1991).
- <sup>33</sup> X. Zhu, P. B. Littlewood, and A. J. Millis, Phys. Rev. B **50**, 4600 (1994).
- <sup>34</sup> M.-C. Cha and H. A. Fertig, Phys. Rev. Lett. **73**, 870 (1994).
- <sup>35</sup> C. Reichhardt, C. J. Olson, N. Grønbech-Jensen, and F. Nori, Phys. Rev. Lett. **86**, 4354 (2001).
- <sup>36</sup> P. Monceau, Adv. Phys. **61**, 325 (2012).
- <sup>37</sup> P. Brussarski, S. Li, S. V. Kravchenko, A. A. Shashkin, and M. P. Sarachik, Nature Commun. **9**, 3803 (2018).
- <sup>38</sup> J. Yoon, C. C. Li, D. Shahar, D. C. Tsui, and M. Shayegan, Phys. Rev. Lett. **82**, 1744 (1999).
- <sup>39</sup> M. S. Hossain, M. K. Ma, K. A. Villegas-Rosales, Y. J. Chung, L. N. Pfeiffer, K. W. West, K. W. Baldwin, and M. Shayegan, Phys. Rev. Lett. **129**, 036601 (2022).
- <sup>40</sup> D. G. Rees, N. R. Beysengulov, J.-J. Lin, and K. Kono, Phys. Rev. Lett. **116**, 206801 (2016).
- <sup>41</sup> A. O. Badrutdinov, A. V. Smorodin, D. G. Rees, J. Y. Lin, and D. Konstantinov, Phys. Rev. B **94**, 195311 (2016).
- <sup>42</sup> J.-Y. Lin, A. V. Smorodin, A. O. Badrutdinov, and D. Konstantinov, Phys. Rev. B **98**, 085412 (2018).
- <sup>43</sup> M. M. Fogler, A. A. Koulakov, and B. I. Shklovskii, Phys. Rev. B **54**, 1853 (1996).
- <sup>44</sup> R. Moessner and J. T. Chalker, Phys. Rev. B **54**, 5006 (1996).
- <sup>45</sup> E. Fradkin and S. A. Kivelson, Phys. Rev. B **59**, 8065 (1999).
- <sup>46</sup> M. P. Lilly, K. B. Cooper, J. P. Eisenstein, L. N. Pfeiffer, and K. W. West, Phys. Rev. Lett. **82**, 394 (1999).
- <sup>47</sup> K. B. Cooper, M. P. Lilly, J. P. Eisenstein, L. N. Pfeiffer, and K. W. West, Phys. Rev. B **60**, R11285 (1999).
- <sup>48</sup> C. Reichhardt, C. J. O. Reichhardt, I. Martin, and A. R. Bishop, Phys. Rev. Lett. **90**, 026401 (2003).
- <sup>49</sup> X. Wang, H. Fu, L. Du, X. Liu, P. Wang, L. N. Pfeiffer, K. W. West, R.-R. Du, and X. Lin, Phys. Rev. B **91**, 115301 (2015).
- <sup>50</sup> C.-C. Li, J. Yoon, L. W. Engel, D. Shahar, D. C. Tsui, and M. Shayegan, Phys. Rev. B **61**, 10905 (2000).
- <sup>51</sup> P. D. Ye, L. W. Engel, D. C. Tsui, R. M. Lewis, L. N. Pfeiffer, and K. West, Phys. Rev. Lett. **89**, 176802 (2002).
- <sup>52</sup> Y. P. Chen, R. M. Lewis, L. W. Engel, D. C. Tsui, P. D. Ye, Z. H. Wang, L. N. Pfeiffer, and K. W. West, Phys. Rev. Lett. **93**, 206805 (2004).
- <sup>53</sup> Y. P. Chen, G. Sambandamurthy, Z. H. Wang, R. M. Lewis, L. W. Engel, D. C. Tsui, P. D. Ye, L. N. Pfeiffer, and K. W. West, Nat. Phys. **2**, 452 (2006).
- <sup>54</sup> J. Jang, B. M. Hunt, L. N. Pfeiffer, K. W. West, and R. C. Ashoori, Nature Phys. **13**, 340 (2017).
- <sup>55</sup> C. Zhang, R.-R. Du, M. J. Manfra, L. N. Pfeiffer, and K. W. West, Phys. Rev. B **92**, 075434 (2015).
- <sup>56</sup> T. Knighton, Z. Wu, J. Huang, A. Serafin, J. S. Xia, L. N. Pfeiffer, and K. W. West, Phys. Rev. B **97**, 085135 (2018).
- <sup>57</sup> M. S. Hossain, M. K. Ma, K. A. Villegas Rosales, and M. Shayegan, Proc. Natl. Acad. Sci. (USA) **117**, 32244 (2020).
- <sup>58</sup> V. Shingla, S. A. Myers, L. N. Pfeiffer, K. W. Baldwin, and G. A. Csáthy, Commun. Phys. **4**, 204 (2021).
- <sup>59</sup> I. Jo, H. Deng, Y. Liu, L. N. Pfeiffer, K. W. West, K. W. Baldwin, and M. Shayegan, Phys. Rev. Lett. **120**, 016802 (2018).
- <sup>60</sup> G. A. Csáthy, D. C. Tsui, L. N. Pfeiffer, and K. W. West, Phys. Rev. Lett. **98**, 066805 (2007).
- <sup>61</sup> P. T. Madathil, K. A. Villegas Rosales, C. Wang, E. Y. Chung, L. N. Pfeiffer, K. Baldwin, K. W. West, and M. Shayegan, Bull. Am. Phys. Soc. **67**, 1141 (2022).
- <sup>62</sup> J. Jaroszyński, D. Popović, and T. M. Klapwijk, Phys. Rev. Lett. **89**, 276401 (2002).
- <sup>63</sup> R. Leturcq, D. L'Hôte, R. Tourbot, C. J. Mellor, and M. Henini, Phys. Rev. Lett. **90**, 076402 (2003).
- <sup>64</sup> J. Jaroszyński, D. Popović, and T. M. Klapwijk, Phys. Rev. Lett. **92**, 226403 (2004).
- <sup>65</sup> E. Abrahams, S. V. Kravchenko, and M. P. Sarachik, Rev. Mod. Phys. **73**, 251 (2001).
- <sup>66</sup> B. Spivak, S. V. Kravchenko, S. A. Kivelson, and X. P. A. Gao, Rev. Mod. Phys. **82**, 1743 (2010).
- <sup>67</sup> C. Reichhardt and C. J. Olson Reichhardt, Phys. Rev. Lett. **93**, 176405 (2004).
- <sup>68</sup> T. Smoleński, P. E. Dolgirev, C. Kuhlenkamp, A. Popert, Y. Shimazaki, P. Back, X. Lu, M. Kroner, K. Watanabe, T. Taniguchi, et al., Nature (London) **595**, 53 (2021).
- <sup>69</sup> H. Li, S. Li, E. C. Regan, D. Wang, W. Zhao, S. Kahn, K. Yumigeta, M. Blei, T. Taniguchi, K. Watanabe, et al., Nature (London) **597**, 650 (2021).
- <sup>70</sup> B. Padhi, C. Setty, and P. W. Phillips, Nano Lett. **18**, 6175 (2018).
- <sup>71</sup> Y. Zhou, J. Sung, E. Brutschea, I. Esterlis, Y. Wang, G. Scuri, R. J. Gelly, H. Heo, T. Taniguchi, K. Watanabe, et al., Nature (London) **595**, 48 (2021).
- <sup>72</sup> B. Padhi, R. Chitra, and P. W. Phillips, Phys. Rev. B **103**, 125146 (2021).
- <sup>73</sup> Y. J. Chung, K. A. Villegas Rosales, K. W. Baldwin, P. T. Madathil, K. W. West, M. Shayegan, and L. N. Pfeiffer, Nature Mater. **20**, 632 (2021).
- <sup>74</sup> M. Shayegan, Nature Rev. Phys. **4**, 212 (2022).
- <sup>75</sup> M.-C. Cha and H. A. Fertig, Phys. Rev. Lett. **73**, 870 (1994).
- <sup>76</sup> C. Reichhardt and C. J. O. Reichhardt, Phys. Rev. B **103**, 125107 (2021).
- <sup>77</sup> C. Reichhardt, C. J. O. Reichhardt, and M. Milosevic, Rev. Mod. Phys. p. in press (2022).
- <sup>78</sup> A. B. Kolton, D. Domínguez, and N. Grønbech-Jensen, Phys. Rev. Lett. **86**, 4112 (2001).
- <sup>79</sup> S. Okuma, Y. Yamazaki, and N. Kokubo, Phys. Rev. B **80**, 220501 (2009).
- <sup>80</sup> T. Sato, A. Kikkawa, Y. Taguchi, Y. Tokura, and F. Kagawa, Phys. Rev. B **102**, 180411 (2020).
- <sup>81</sup> K. Bennaceur, C. Lupien, B. Reulet, G. Gervais, L. N. Pfeiffer, and K. W. West, Phys. Rev. Lett. **120**, 136801

- (2018).
- <sup>82</sup> M. Palassini and M. Goethe, *J. Phys.: Conf. Ser.* **376**, 012009 (2012).
- <sup>83</sup> C. J. Olson, C. Reichhardt, and F. Nori, *Phys. Rev. B* **56**, 6175 (1997).
- <sup>84</sup> K. E. Bassler and M. Paczuski, *Phys. Rev. Lett.* **81**, 3761 (1998).
- <sup>85</sup> S. A. Díaz, C. Reichhardt, D. P. Arovas, A. Saxena, and C. J. O. Reichhardt, *Phys. Rev. Lett.* **120**, 117203 (2018).
- <sup>86</sup> P. G. Baity, T. Sasagawa, and D. Popović, *Phys. Rev. Lett.* **120**, 156602 (2018).
- <sup>87</sup> O. Perković, K. Dahmen, and J. P. Sethna, *Phys. Rev. Lett.* **75**, 4528 (1995).
- <sup>88</sup> C. Reichhardt and C. J. O. Reichhardt, *Phys. Rev. Lett.* **103**, 168301 (2009).
- <sup>89</sup> T. Kaji, S. Maegochi, K. Ienaga, S. Kaneko, and S. Okuma, *Sci. Rep.* **12**, 1542 (2022).